Article

Late Ordovician High Ba-Sr intrusion in the Eastern North Qilian Orogen: Implications for Crust-Mantle Interaction and Proto-Tethys Ocean Evolution

Shaoqing Zhao [1,*], Lianfu Hai [2,3], Bin Liu [1], Huan Dong [1], Chao Mei [2,3], Qinghai Xu [1], Caixia Mu [2,3] and Xiangcheng Wei [2,3]

[1] School of Geosciences, Yangtze University, Wuhan 430100, China
[2] Mineral Geological Survey Institute of Ningxia Hui Autonomous Region, Yinchuan 750021, China
[3] Institute of Mineral Geology of Ningxia Hui Autonomous Region, Yinchuan 750021, China
* Correspondence: shaoqing@yangtzeu.edu.cn

Abstract: The petrogenesis of high Ba-Sr granitoids provide a great significance to penetrate the Proto-Tethys evolution in the North Qilian orogenic belt. This paper presents a combination of zircon U-Pb age, whole-rock major and trace element concentrations, and Sr-Nd-Hf isotopic data for Caowa high Ba-Sr dioritic intrusion from the eastern part of the North Qilian orogenic belt, aiming to decipher its petrogenesis and tectonic setting. LA-ICP-MS zircon U-Pb dating yields an emplacement age of 447 ± 3 Ma for the Caowa intrusion, indicating a magmatic activity of the late Ordovician. The Caowa quartz diorites contain moderate contents of SiO_2, MgO, $Mg^{\#}$ and resultant high concentrations of $Na_2O + K_2O$, $Fe_2O_3^T$ and Al_2O_3, displaying calc-alkaline and metaluminous characteristics. Their relatively elevated Ba (up to 1165 ppm) and Sr (561 to 646 ppm) contents, with obvious enrichment in LILEs (e.g. Ba, Th, U) and depletion in HFSEs (e.g. Nb, Ta, Ti) resemble those of typical high Ba-Sr granitoids in subduction zone. Together with enriched Sr-Nd isotopic compositons[$(^{87}Sr/^{86}Sr)_I$ = 0.7082–0.7086, $\varepsilon_{Nd}(t)$ = −5.1 to −4.9], and relatively extensive $\varepsilon_{Hf}(t)$ values (−13.2 to +8.5) of zircons, it suggests that these high Ba-Sr quartz diorites were derived from a mixture magma source between the ancient crust materials and the enriched lithospheric mantle metasomatised by fluid was released from subducted oceanic crust or sediment. Taking into account the ophiolites, high pressure metamorphic rocks and arc magmatic rocks in the region, we infer that affected by the northward subduction of the Qilian Proto-Tethys ocean, the Laohushan oceanic crust of the North Qilian back-arc basin was subducted during the Late Ordovician and resulted in extensive metasomatism of lithospheric mantle by fluids derived from oceanic crust or sediments, and the Caowa high Ba-Sr quartz diorites generated in the process of crust-mantle interaction during the Late Ordovician.

Keywords: High Ba-Sr granitoids; Late Ordovician; Subduction; Proto-Tethys; North Qilian orogen

1. Introduction

The Qilian orogenic system, located in the northeastern Tibetan Plateau, has been considered as the northernmost orogenic collage of the Proto-Tethys Realm. It records a multistage tectonic processes from the Neo-proterozoic continental breakup, the Early Paleozoic oceanic subduction and accretion, finally resulting in arc-continent and continent collisions [1–3]. As a significant unit of the Qilian orogenic system, the North Qilian orogenic belt has been confirmed by a typical subduction-accretion suture with a complex trough-arc-basin system, marking the tectonic evolution of Proto-Tethys ocean [4–6]. Previous studies have been carried out on the distribution of Early Paleozoic mid-ocean-ridge type ophiolites, high-pressure metamorphic rocks (e.g., eclogites and blueschists), subduction/collision-related arc magmatic rocks and back-arc basin ophiolites in the North

 doi:10.20944/preprints202305.0763.v1

Qilian from south to north, and northward subduction of the Qilian Proto-Tethys ocean during the Ordovician was basically authenticated [5,7–9]. Nevertheless, the evolution process of Proto-Tethys ocean in the eastern part of North Qilian belt remains unclear. There are many Early Paleozoic adakitic granitoids have been recognized in the Eastern North Qilian orogenic belt, and some recent studies suggested that they generated during continent-continent collision or post-collision collapse [10–14]. However, their petrogenesis and tectonic settings are still debated and little research has focused on the oceanic subduction-related granitoids (e.g., I-type granite, high Ba-Sr granitic rocks) in the region, especially in the Nanhuashan area of Ningxia province, easternmost of the North Qilian belt.

High Ba-Sr granitoids, as a distinct group of magmatic rocks, are widespread in Phanerozoic orogenic systems and provide important insights into the deep geodynamic process of orogenic belts [15–18]. Compared to traditional I-, S- and A-type granitoids, the high Ba-Sr granitoids are characterized by alkali-rich, high Ba (> 500 ppm) and Sr (> 300 ppm) contents, and low Rb (< 200 ppm) and Y (< 30 ppm) contents with Rb/Ba ratios < 0.2. They also display high Sr/Y ratios, enrichment of light rare earth (LREE) and large-ion lithophile elements (LILE), depletion in heavy rare earth (HREE) and high field-strength elements (HFSE), with no significant negative Eu anomalies[15,19]. High Ba-Sr granitoids always carry geochemical and isotopic signatures of enriched mantle sources, which was linked to the oceanic subduction-related metasomatism[16,20–24]. However, the possible mechanisms for the generation of high Ba-Sr granitoids, such as partial melting of subducted ocean islands/ocean plateaus[15], melting of mafic lower crust[19,25], or magma mixing[17,26], have also been proposed. Therefore, the recognition of high Ba-Sr granitoids may provides particular information on the crust-mantle interactions and the growth of the continental crust in subduction zones.

In this contribution, we present zircon U-Pb geochronology, whole-rock geochemistry and Sr-Nd-Hf isotopic data for the Late Ordovician dioritic intrusion (mainly composed of quartz diorites) with high Ba-Sr signatures in the Nanhuashan area of Ningxia, Eastern North Qilian orogenic belt (Figure 1). These results, together with previously published data, are used to elucidate the petrogenesis of the high Ba-Sr quartz diorites, and further evaluate their geodynamic implications for the Proto-Tethys Ocean evolution.

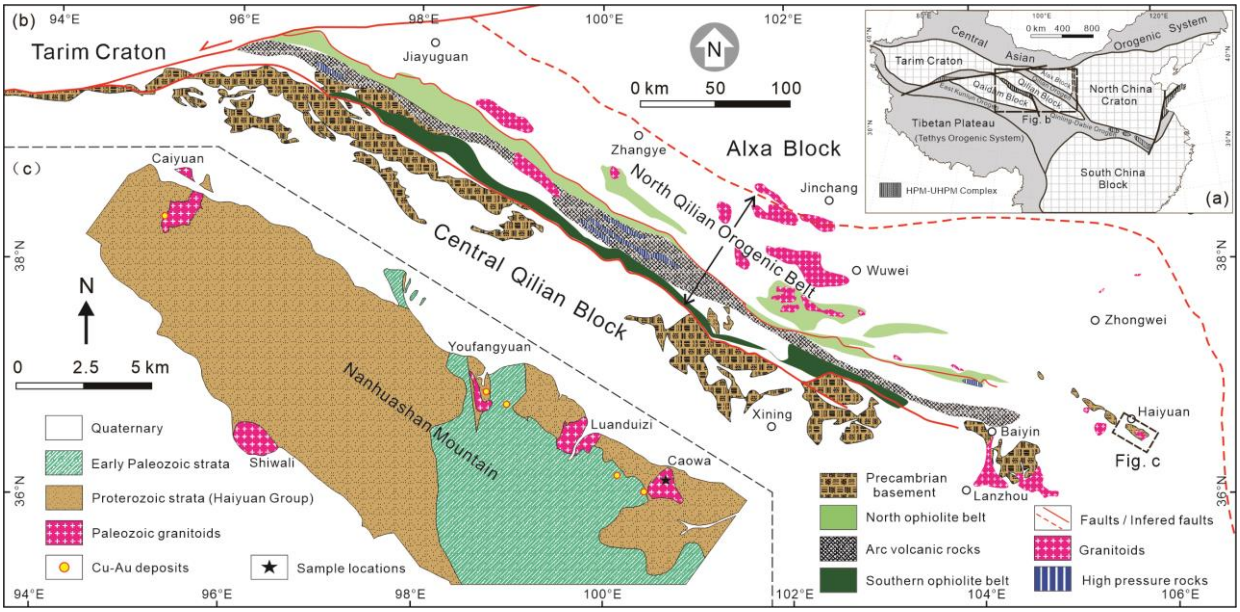

Figure 1. (a) Tectonic sketch map of China (modified from [5]); (b) Simplified geological map of the North Qilian Orogenic Belt showing distributions of the main tectonic units (modified from [29]), and (c) simplified distribution map of the Caowa dioritic intrusion, showing the studied sample's location.

 doi:10.20944/preprints202305.0763.v1

2. Geological Background and Petrography

The Qilian orogenic belt, located in the northeastern margin of the Tibetan Plateau, has traditionally been regarded as an important part of the Central China orogenic belt (Figure 1a). It is sequentially divided into three units from north to south: the North Qilian orogenic belt (NQOB), the Central Qilian block, and the South Qilian accretionary complex belt[1,27]. The NQOB, extending NW-SE more than 1000 km, lies between the Alxa Block to the north and the Qilian Block to the south, and is separated from the Altyn-Tagh Fault to the west (Figure 1b). It is dominated by an outcrop of Early Paleozoic ophiolites, high-pressure metamorphic rocks and a series of subduction/collision-related magmatic rocks, and is considered to be a typical subduction-accretion orogenic belt with a complex trough-arc-basin system[5,6]. Two ophiolite sequences are distributed in the NQOB (Figure 1b). The southern ophiolite belt (550−496 Ma) is connected with Aoyougou, Yushigou and Dongcaohe ophiolites, mainly consists of mantle peridotite, cumulate gabbro and mid-ocean ridge basalt (MORB), which documented the oceanic crust fragments of the Qilian Proto-Tethys ocean[5]. The northern ophiolite belt (490−448 Ma) is a typical back-arc basin ophiolite (e.g., Jiugequan, Biandukou and Laohushan ophiolites), representing the extension of the North Qilian back-arc oceanic basin[5,28,29]. There is a volcanic-magma arc belt (520−440 Ma) outcrops between the two ophiolite belts, mainly including mafic and felsic volcanic rocks[8]. The high pressure-low temperature (HP-LT) metamorphic rocks in the NQOB are predominantly composed of blueschists and low-temperature eclogites, with the metamorphic ages ranging fom 490 to 440 Ma[2,30,31]. In addition, a large number of Early Paleozoic granitoids (520−420 Ma), including adakitic, I- and A-type granitoids, have been recognized in the NQOB from Changma-Dachadaban-Corridor Nanshan in the west to Leigongshan - Laohushan - Quwushan Mountain in the east, and their formation was linked to oceanic subduction, closure and post collision processes of the Qilian Proto-Tethys Ocean[11,13,14,32,33].

The Nanhuashan Mountain, connecting with Quwushan - Baojishan - Laohushan - Leigongshan Mountain to the west in the eastern part of NQOB, is developed many Early Paleozoic granitic intrusions. These intrusions, including Caiyuan, Shiwali, Youfangyuan, Luanduizi and Caowa intrusions, intrude into the Meso-proterozoic Haiyuan Group and they are closely related to regional Cu-Au mineralization. The high Ba-Sr signature rocks reported in this paper were collected from the Caowa intrusion (Figure 1c). The Caowa intrusion consists of quartz diorites, with an outcrop area of ~4 km^2, which are medium- to coarse-grained rocks (Figure 2a). The quartz diorites are mainly composed of plagioclase (40–50 vol.%), hornblende (20–30 vol.%), quartz (5–10 vol.%), and K-feldspar (5–10 vol.%), with minor amounts of iron oxides, zircon, and apatite (Figure 2b–d). The plagioclase generally forms euhedral-subhedral laths with polysynthetic twinning. Some of these laths display concentric compositional zoning and have more sericitized (Figure 2b, d). Hornblende occurs as euhedral-subhedral grains, with length of 0.5–1 mm, and usually appears as a mafic polycrystalline agglomerate (Figure 2c,d). K-feldspar is subhedral-anhedral, mainly consists of orthoclase and occasional microcline. Quartz is anhedral and fills the interstices between amphibole and plagioclase crystals. In addition, acicular apatite commonly occurs nearby the hornblende polycrystalline agglomerate (Figure 2c,d).

 doi:10.20944/preprints202305.0763.v1

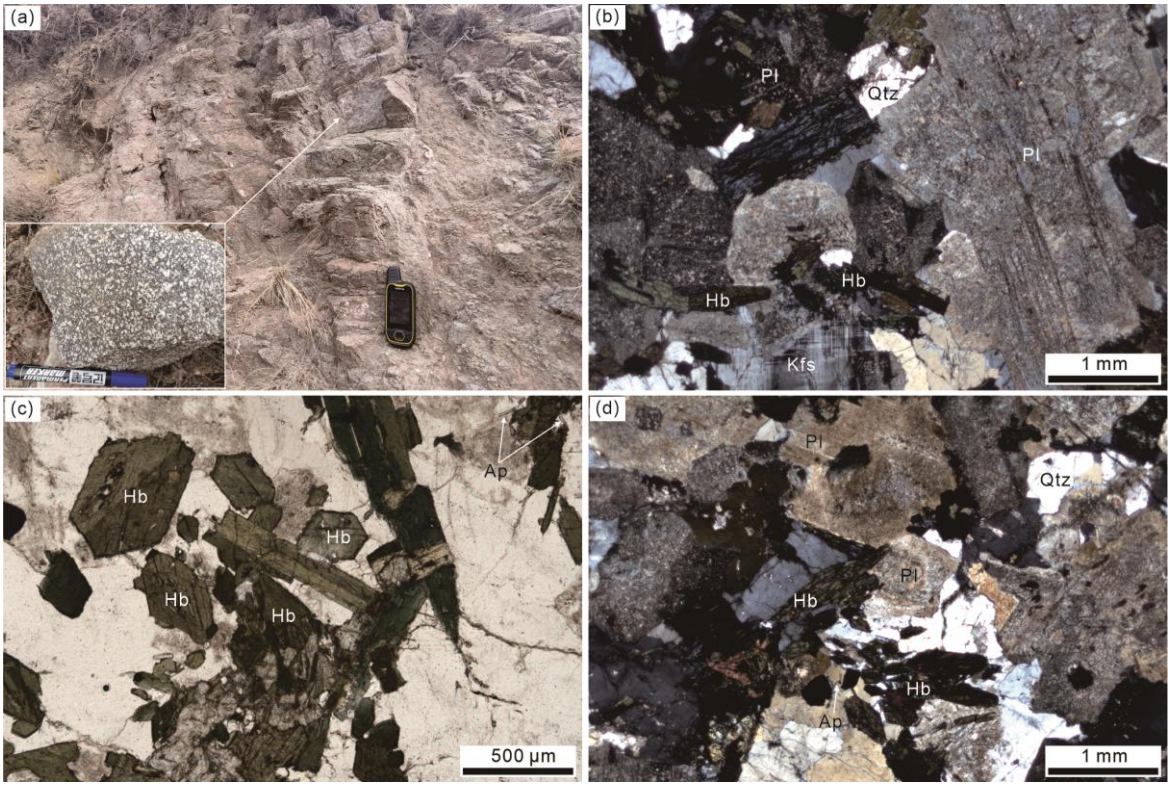

Figure 2. Field and microscope photographs of the Caowa dioritic intrusion in the Eatern NQOB. (**a**) Field photograph of the dioritic intrusion; (**b–d**) Photomicrographs of the quartz diorites. Abbreviations: Hb = hornblende, Pl = plagioclase, Kfs = K-feldspar, Qtz = quartz, Ap = apatite.

3. Analytical Methods

3.1. Zircon U-Pb Dating and Hf Isotope Analyses

U-Pb dating and trace element analysis of zircon were simultaneously conducted by LA-ICP-MS at the Wuhan SampleSolution Analytical Technology (Wuhan, China). Laser sampling was performed using a GeolasPro laser ablation system that consists of a COMPexPro 102 ArF excimer laser (wavelength of 193 nm and maximum energy of 200 mJ) and a MicroLas optical system. An Agilent 7900 ICP-MS instrument was used to acquire ion-signal intensities. Helium was applied as a carrier gas. Argon was used as the make-up gas and mixed with the carrier gas via a T-connector before entering the ICP. A "wire" signal smoothing device is included in this laser ablation system[34]. The spot size and frequency of the laser were set to 32 μm and 8 Hz, respectively. Zircon 91,500 and glass NIST610 were used as external standards for U-Pb dating and trace element calibration, respectively. Each analysis incorporated a background acquisition of approximately 20-30 s followed by 50 s of data acquisition from the sample. Detailed operating conditions for the laser ablation system and the ICP-MS instrument and data reduction are the same as description by Zong et al. (2017) [35]. An Excel-based software ICPMSDataCal was used to perform off-line selection and integration of background and analyzed signals, time-drift correction and quantitative calibration for trace element analysis and U-Pb dating [36]. Concordia diagrams and weighted mean calculations were made using Isoplot/Ex_ver3[37].

Zircon Hf isotope analyses were conducted using a Neptune Plus MC-ICP-MS (Thermo Fisher Scientific, Germany) in combination with a Geolas HD excimer ArF laser ablation system (Coherent, Göttingen, Germany) that was hosted at the Wuhan SampleSolution Analytical Technology. The sampling spot size was 32 μm and the energy density was ~7.0 J cm^{-2} during the analyses. Detailed operating conditions for the laser ablation system and the MC-ICP-MS instrument and analytical method are the same as description

 doi:10.20944/preprints202305.0763.v1

by Hu et al. (2012) [38]. In order to ensure the reliability of the analysis data, three international zircon standards of Plešovice, 91,500 and GJ-1 are analyzed simultaneously with the actual samples. The Hf isotope compositions of Plešovice, 91,500 and GJ-1 are 0.282478 ± 0.000008, 0.282300 ± 0.000011 and 0.282009 ± 0.000010, respectively [39].

3.2. Whole-Rock Major and Trace Elements Analyses

Major and trace elements analyses of the fresh whole-rock samples were carried out at Wuhan SampleSolution Analytical Technology. The major element analyses were conducted using Zsx Primus II wavelength dispersive X-ray fluorescence spectrometer (XRF) and the relative standard deviation is less than 2%. The trace elements were analysed on an Agilent 7700e ICP-MS. The sample powder was accurately weighed and placed in a Teflon bomb after drying for 12 h in an oven at 105 °C. The sample powders were then digested in an HF + HNO_3 solution in Teflon bombs, which were then placed in a stainless-steel pressure jacket and heated to 190 °C in an oven for >24 h. The final solution was transferred to a polyethylene bottle and diluted to 100 g by the addition of 2% HNO_3.

3.3. Whole-Rock Sr-Nd Isotope Analyses

Whole-rock Sr-Nd isotope analyses were measured on a Neptune Plus MC-ICP-MS (Thermo Fisher Scientific, Dreieich, Germany) at Wuhan SampleSolution Analytical Technology. The Sr and Nd fractions were eluted using 2.5 and 0.3 M HCl, respectively, and gently evaporated to dryness prior to mass-spectrometric measurement. International standards of NBS987 and GSB were used as bracketing standards to monitor the instrument drift during the analysis of Sr and Nd isotopes, respectively. Repeated analysis for NBS987 gives an average $^{87}Sr/86Sr = 0.710242 \pm 14$ (2σ). Repeated analysis for GSB gives an average $^{143}Nd/^{144}Nd = 0.512440 \pm 1$ (2σ).

4. Results

4.1. Zircon U–Pb Geochronology

LA-ICP-MS zircon U-Pb isotopic data and trace element results are listed in Tables 1 and 2, respectively. Representative CL images and concordia diagrams are shown in Figure 3.

Table 1. LA-ICP-MS zircon U-Pb dating results of the Caowa quartz diorite.

Spot No.	Contents (ppm)		Th/U	Isotopic Ratios								Isotopic Ages (Ma)					
	^{232}Th	^{238}U		$^{207}Pb/^{206}Pb$	1σ	$^{207}Pb/^{235}U$	1σ	$^{206}Pb/^{238}U$	1σ	$^{208}Pb/^{232}Th$	1σ	$^{207}Pb/^{206}Pb$	1σ	$^{207}Pb/^{235}U$	1σ	$^{206}Pb/^{238}U$	1σ
CW-6-01	744	1889	0.39	0.0546	0.0018	0.5629	0.0146	0.0730	0.0012	0.0224	0.0005	394	79	453	10	454	7
CW-6-02	1093	2859	0.38	0.0602	0.0013	0.5984	0.0127	0.0721	0.0008	0.0247	0.0006	613	46	476	8	449	5
CW-6-03	781	2046	0.38	0.0559	0.0013	0.5572	0.0121	0.0709	0.0007	0.0215	0.0004	456	52	450	8	442	4
CW-6-04	744	1860	0.40	0.0559	0.0013	0.5516	0.0114	0.0712	0.0008	0.0219	0.0004	456	52	446	7	444	5
CW-6-05	370	1424	0.26	0.0538	0.0013	0.5396	0.0132	0.0725	0.0007	0.0213	0.0004	365	54	438	9	451	4
CW-6-06	619	1916	0.32	0.0561	0.0013	0.5718	0.0168	0.0734	0.0009	0.0225	0.0004	457	52	459	11	457	5
CW-6-07	368	1498	0.25	0.0599	0.0012	0.5898	0.0120	0.0712	0.0006	0.0251	0.0004	611	38	471	8	444	3
CW-6-08	465	1687	0.28	0.0557	0.0010	0.5507	0.0110	0.0715	0.0007	0.0218	0.0004	443	43	445	7	445	4
CW-6-09	342	1222	0.28	0.0560	0.0012	0.5480	0.0117	0.0708	0.0006	0.0220	0.0004	450	46	444	8	441	4
CW-6-10	516	1633	0.32	0.0562	0.0018	0.5645	0.0180	0.0728	0.0008	0.0228	0.0005	457	72	454	12	453	5
CW-6-11	393	1455	0.27	0.0577	0.0020	0.5787	0.0200	0.0723	0.0008	0.0272	0.0007	520	74	464	13	450	5
CW-6-12	761	2264	0.34	0.0559	0.0013	0.5637	0.0135	0.0727	0.0006	0.0212	0.0004	456	50	454	9	452	4
CW-6-13	494	1690	0.29	0.0553	0.0012	0.5519	0.0128	0.0719	0.0007	0.0230	0.0005	433	48	446	8	448	4
CW-6-14	428	1386	0.31	0.0561	0.0014	0.5554	0.0135	0.0716	0.0007	0.0221	0.0005	457	21	449	9	446	4
CW-6-15	615	1777	0.35	0.0556	0.0014	0.5521	0.0159	0.0714	0.0006	0.0226	0.0005	435	56	446	10	444	4
CW-6-16	451	1584	0.28	0.0558	0.0012	0.5587	0.0122	0.0722	0.0006	0.0216	0.0004	443	51	451	8	449	4
CW-6-17	495	1491	0.33	0.0571	0.0019	0.5540	0.0185	0.0700	0.0009	0.0233	0.0006	498	74	448	12	436	5
CW-6-18	608	1693	0.36	0.0621	0.0020	0.6192	0.0221	0.0718	0.0009	0.0242	0.0012	676	69	489	14	447	5
CW-6-19	487	1678	0.29	0.0563	0.0014	0.5778	0.0141	0.0737	0.0008	0.0233	0.0006	465	54	463	9	459	5

Preprints (www.preprints.org) | NOT PEER-REVIEWED | Posted: 10 May 2023 doi:10.20944/preprints202305.0763.v1

Table 2. Zircon trace element data of the Caowa quartz diorite.

Spot No.	La	Ce	Pr	Nd	Sm	Eu	Gd	Tb	Dy	Ho	Er	Tm	Yb	Lu	Eu/Eu*	Hf	Ta	Y	Ti	Nb
CW-6-01	0.16	65.71	0.30	2.50	5.64	3.43	41.79	15.29	207	88.11	442	106.56	1095	257	0.49	28295	6.09	2803	13.32	18.18
CW-6-02	2.71	95.28	2.51	16.76	13.22	6.67	59.00	21.00	273	113.41	556	132.00	1356	306	0.62	27149	8.94	3634	22.20	33.09
CW-6-03	0.01	66.60	0.08	1.92	6.56	3.44	42.17	16.44	217	91.56	472	113.50	1184	277	0.48	28530	6.55	2957	11.24	19.62
CW-6-04	0.20	76.26	0.21	3.53	6.55	4.17	44.84	17.58	227	97.89	498	118.97	1248	292	0.55	27469	6.58	3153	12.14	22.23
CW-6-05	0.02	50.15	0.11	1.65	4.07	2.80	30.96	13.94	189	80.95	418	102.28	1088	261	0.54	27647	5.66	2607	9.11	15.53
CW-6-06	13.94	82.46	4.87	22.53	7.96	3.02	38.18	13.71	181	76.11	395	94.46	1003	239	0.44	29534	5.88	2473	7.24	17.51
CW-6-07	2.96	62.56	1.85	11.27	10.34	4.18	41.91	14.74	210	92.24	490	122.45	1296	311	0.53	29319	6.04	3019	13.23	18.31
CW-6-08	0.00	60.01	0.09	2.03	6.29	3.34	44.66	16.44	239	108.89	573	139.26	1488	355	0.45	28350	6.75	3530	10.76	23.00
CW-6-09	0.01	51.36	0.11	2.37	5.80	3.42	40.01	15.27	228	100.04	538	131.31	1376	327	0.51	27151	5.18	3246	11.26	18.19
CW-6-10	0.06	55.93	0.15	2.10	4.98	3.37	36.84	14.65	201	85.35	452	110.00	1156	273	0.55	28330	6.46	2800	11.83	19.52
CW-6-11	1.61	82.48	1.61	11.68	10.50	4.74	42.03	14.21	192	83.62	420	98.51	1029	252	0.60	29354	4.25	2626	22.40	13.69
CW-6-12	0.08	60.44	0.08	1.06	4.83	3.30	35.79	13.82	191	83.22	420	102.55	1069	252	0.55	29612	7.33	2661	9.38	19.93
CW-6-13	0.01	62.43	0.11	2.33	6.54	3.99	45.41	18.07	254	114.76	605	150.52	1592	380	0.52	27316	6.95	3712	13.38	22.66
CW-6-14	1.56	56.25	0.78	6.05	6.50	3.42	40.46	15.75	209	92.13	485	117.96	1243	297	0.49	27661	5.72	2963	30.72	17.65
CW-6-15	0.40	62.18	0.30	2.90	6.80	3.51	42.94	15.20	214	91.05	469	113.20	1174	280	0.48	27915	6.77	2907	10.23	19.48
CW-6-16	0.01	53.87	0.11	2.03	5.84	2.90	38.17	15.39	211	94.62	492	120.89	1268	304	0.45	28605	6.03	3029	11.04	20.50
CW-6-17	0.19	57.12	0.20	2.29	5.43	2.38	32.30	12.46	165	70.94	370	88.25	928	220	0.43	28248	5.33	2278	21.60	13.96
CW-6-18	4.17	127.01	4.87	31.21	23.26	12.35	68.83	21.36	245	98.51	473	107.22	1144	262	0.87	26455	6.09	3042	15.51	18.31
CW-6-19	0.03	55.17	0.09	1.80	5.20	3.05	39.80	15.83	224	99.35	531	132.58	1388	334	0.46	28114	6.50	3256	10.68	21.27

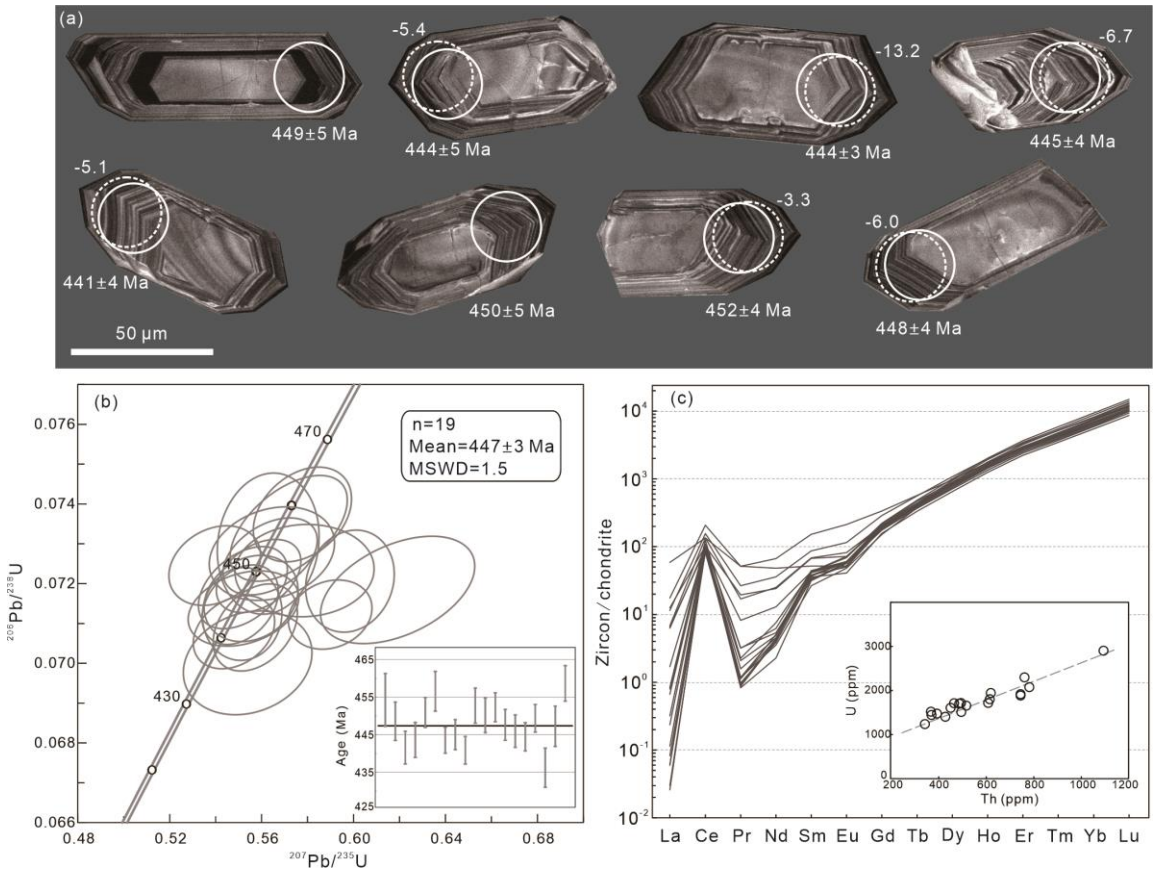

Figure 3. Cathodoluminescence images (**a**), LA-ICP-MS U–Pb concordia diagram (**b**), and chondrite-normalized REE patterns (**c**) of representative zircons from Caowa quartz diorite (**a**). Solid and dashed circles indicate the location of U–Pb analysis and Hf analysis, respectively.

Zircon grains from the Caowa quartz diorite sample CW-6 are colorless to faint yellow, transparent and euhedral morphology. They have a size range of 50–150 μm, with a length/width ratio of 2:1 to 3:1, and show broad oscillatory growth zoning or are

 doi:10.20944/preprints202305.0763.v1

homogeneous in the CL images (Figure 3a). The analyzed zircons have U and Th contents of 1222–2859 and 342–1093 ppm, and show high Th/U ratios ranging from 0.25 to 0.40. They display enrichment in HREE and depletion in LREE, with obvious positive Ce anomalies, weak negative Eu anomalies and positive correlation between Th and U contents (Figure 3c), indicating their magmatic origin [40,41]. Nineteen spots were analyzed on 19 zircons and give $^{206}Pb/^{238}U$ ages ranging from 436 ± 5 to 459 ± 5 Ma. All of the analyses are nearly concordant, yielding a weighted age of 447 ± 3 Ma (MSWD = 1.5) (Figure 3b), which represents the emplacement age of the Caowa dioritic intrusion.

4.2. Whole-Rock Major and Trace Elements

Major and trace element data for the Caowa quartz diorites are listed in Table 3. Based on petrographic examination, all samples are not significantly affected by hydrothermally alternation, and their low loss on ignition (LOI) contents (1.36–2.45 wt.%, Table 3) further indicate that the samples are basically fresh.

Table 3. Major (wt.%), trace element (ppm) and Sr-Nd isotopic compositions of the Caowa quartz diorites.

Sample	CW-1	CW-2	CW-3	CW-4	CW-5	CW-6
SiO_2	62.80	62.87	59.75	58.34	57.53	61.97
TiO_2	0.61	0.59	0.74	0.77	0.90	0.63
Al_2O_3	16.32	16.85	16.99	16.66	17.16	16.90
$Fe_2O_3^T$	5.39	5.22	6.58	6.63	7.88	5.54
MnO	0.13	0.12	0.14	0.14	0.17	0.12
MgO	2.13	2.10	2.43	2.63	3.01	2.08
CaO	3.47	3.71	4.65	5.46	5.26	3.81
Na_2O	3.91	3.95	3.78	3.71	3.65	3.86
K_2O	2.95	2.93	2.78	2.94	2.50	2.82
P_2O_5	0.19	0.19	0.23	0.23	0.26	0.20
LOI	2.13	1.36	1.42	2.453	1.43	1.62
Total	100.03	99.90	99.48	99.97	99.74	99.56
Mg#	44	44	42	44	43	43
A/CNK	1.02	1.02	0.96	0.87	0.94	1.03
Na_2O+K_2O	6.86	6.89	6.55	6.65	6.16	6.68
Sc	9.22	8.41	11.84	11.76	15.11	9.24
V	78.3	80.2	105.7	106.7	130.8	83.7
Cr	4.81	5.21	5.69	5.45	6.43	4.58
Co	8.92	9.08	11.92	11.89	14.65	9.57
Ni	3.29	3.46	4.53	4.61	5.12	3.71
Cu	9.87	8.70	11.77	14.24	23.66	4.63
Zn	70.0	69.0	80.5	78.6	93.0	67.9
Rb	92.1	90.0	81.6	80.2	76.6	72.9
Sr	561	612	623	601	646	646
Y	25.07	22.93	28.90	28.01	33.24	23.98
Zr	193.6	180.5	218.9	206.7	228.8	193.5
Nb	12.53	13.02	13.42	13.84	13.05	12.20
Ba	1165	916	860	1151	822	902
La	60.86	40.90	27.52	18.27	57.29	44.74
Ce	112.96	77.92	53.83	37.62	111.28	85.59
Pr	12.26	8.69	6.64	5.05	12.74	9.50
Nd	41.73	30.58	25.94	21.20	45.27	33.69
Sm	7.06	5.42	5.92	5.23	8.40	6.20

 doi:10.20944/preprints202305.0763.v1

Eu	1.58	1.36	1.60	1.57	1.96	1.54
Gd	5.04	4.30	5.20	4.96	6.60	4.66
Tb	0.74	0.64	0.81	0.79	1.00	0.70
Dy	4.30	3.70	4.92	4.67	5.89	3.98
Ho	0.86	0.79	0.96	1.00	1.17	0.83
Er	2.59	2.32	2.93	2.87	3.32	2.50
Tm	0.37	0.34	0.44	0.42	0.48	0.37
Yb	2.50	2.37	2.86	2.87	3.17	2.38
Lu	0.39	0.36	0.44	0.43	0.49	0.37
Hf	5.02	4.60	5.44	5.11	5.71	4.76
Ta	0.76	0.90	0.80	0.81	0.65	0.73
Pb	21.10	18.48	15.75	18.52	17.27	19.10
Th	15.53	10.99	6.12	4.29	14.31	11.99
U	1.68	1.39	1.57	1.68	2.17	1.79
REE	253.22	179.69	140.01	106.95	259.06	197.05
Eu/Eu*	0.77	0.83	0.86	0.93	0.78	0.84
Sr/Y	22.38	26.68	21.57	21.44	19.44	26.93
Nb/Ta	16.38	14.46	16.70	16.99	20.22	16.70
$(La/Yb)_N$	17.47	12.36	6.91	4.56	12.95	13.47
$(Gd/Yb)_N$	1.67	1.50	1.51	1.43	1.72	1.62
$^{87}Rb/^{86}Sr$		0.4258		0.3863		0.3267
$^{87}Sr/^{86}Sr$		0.711129		0.710716		0.710747
$(^{87}Sr/^{86}Sr)_i$		0.708338		0.708184		0.708606
$^{147}Sm/^{144}Nd$		0.1071		0.1493		0.1113
$^{143}Nd/^{144}Nd$		0.512124		0.512243		0.512119
$\varepsilon_{Nd}(t)$		-4.8		-4.9		-5.1
T_{DM2} (Ma)		1579		1591		1607

The Caowa quartz diorites have a relatively variable SiO_2 contents (57.53 to 62.87 wt.%) and are of intermediate diorite or monzonite compositions (Figure 4a). They have definite high-K calc-alkaline and metaluminous to weak peraluminous features, as indicated by their high total alkalis ($Na_2O + K_2O$ = 6.16–6.89 wt.%), and relatively low A/CNK values (0.87–1.03) (Figure 4b-d). They have high $Fe_2O_3^T$ (5.22–7.88 wt.%), CaO (3.47–5.46 wt.%) contents, and moderate MgO (2.08–3.01 wt.%) contents and $Mg^{\#}$ (42–44). The Caowa quartz diorites have higher contents of REE, ranging from 106.95 to 259.06 ppm (Table 3). They display slightly high La (18.27–60.86 ppm) and relatively low Yb (2.37–3.17 ppm), yielding the $(La/Yb)_N$ ratios of 4.56–17.47 (Table 3). All samples show similar chondrite-normalized REE patterns and have clearly fractionated LREE relative to HREE, with no significant negative Eu anomalies (Eu/Eu* = 0.77–0.93; Figure 5a). The Caowa quartz diorites display extremely high Ba (up to 1165 ppm) and Sr (561 to 646 ppm) contents, with obvious enrichment in LILEs (Ba, Th, U and K) and depletion in HFSEs (Nb, Ta, Ti and P; Figure 5b).

Preprints (www.preprints.org) | NOT PEER-REVIEWED | Posted: 10 May 2023 doi:10.20944/preprints202305.0763.v1

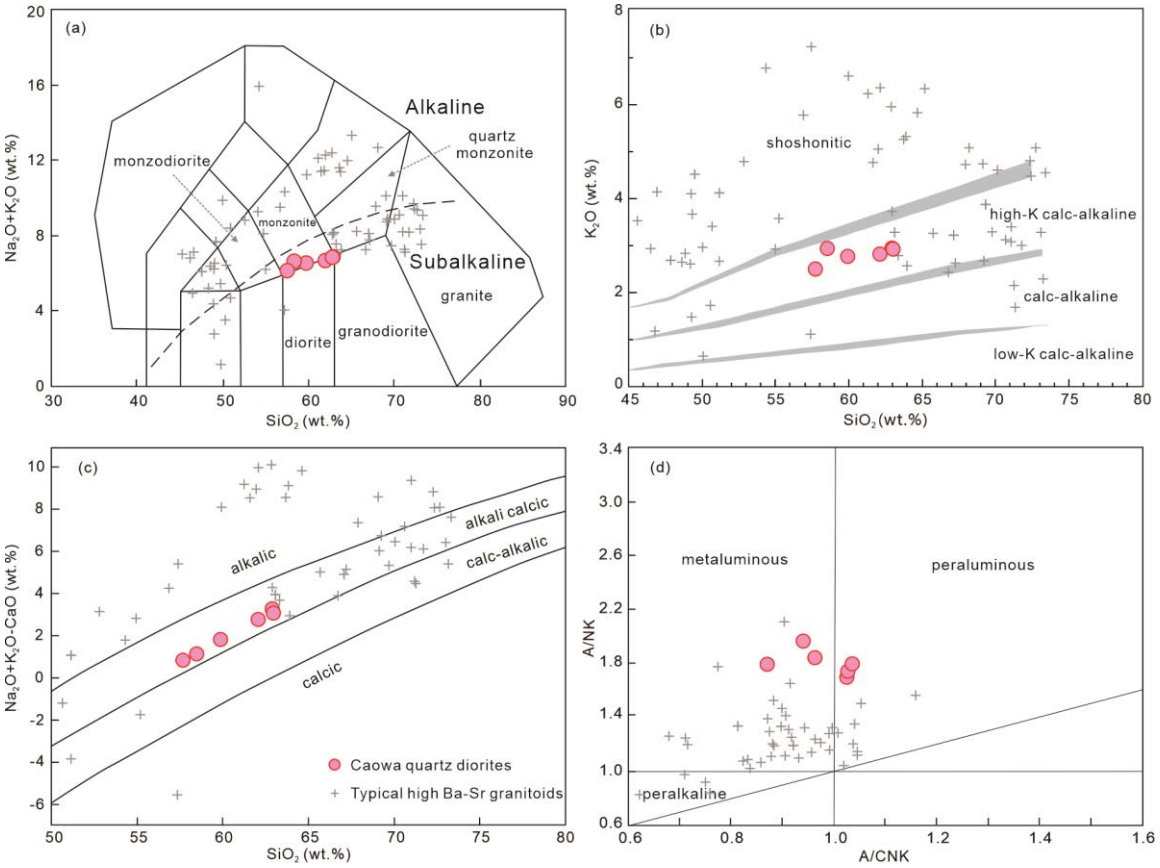

Figure 4. Geochemical classification of the Caowa quartz diorites. (**a**) Total alkali vs. silica (TAS) diagram (after [66]); (**b**) K_2O vs. SiO_2 diagram (after [67]); (**c**) ($Na_2O + K_2O - CaO$) vs. SiO_2 diagram (after [68]); and (**d**) A/NK [molar ratio $Al_2O_3/(Na_2O+K_2O)$] vs. A/CNK [molar ratio $Al_2O_3/(CaO+Na_2O+K_2O)$] diagram (after [69]). The data for typical high Ba-Sr granitoids are from [16,20].

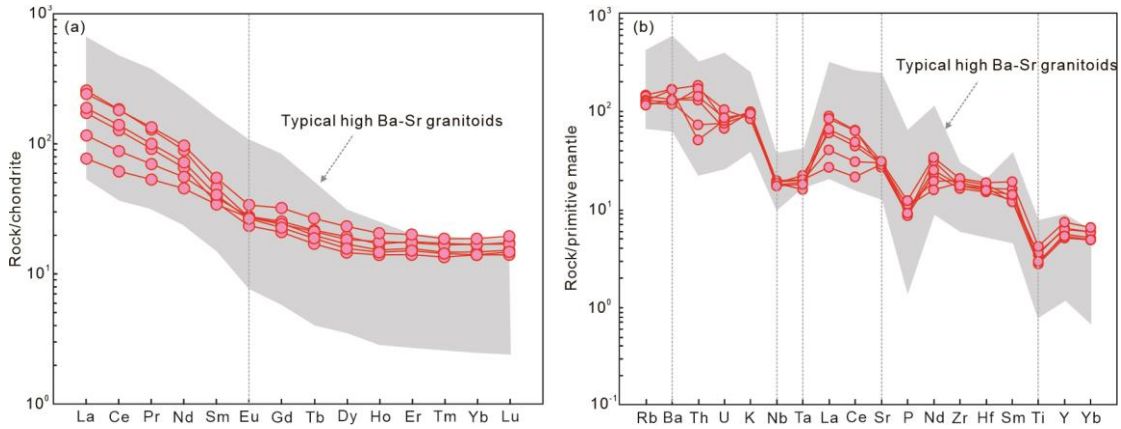

Figure 5. Chondrite-normalized REE patterns (**a**) and primitive mantle-normalized trace element patterns (**b**) for the Caowa quartz diorites. Normalizing values are from [52]. The compositions for typical high Ba-Sr granitoids are from [16,20].

4.3. Whole Rock Sr-Nd Isotopes

Whole rock Sr-Nd isotopic data for selected samples are presented in Table 3 and shown in Figure 6. The initial Sr-Nd isotopic ratios were calculated at 447 Ma based on the zircon U-Pb age. The Caowa quartz diorites show heterogeneous Sr-Nd isotope compositions characterized by slight high $(^{87}Sr/^{86}Sr)_i$ ratios (0.70818–0.70860), and a little low $\varepsilon_{Nd}(t)$ values (-5.1 to -4.9), with two-stage Nd model ages (T_{DM2}) of 1579–1607 Ma.

Preprints (www.preprints.org) | NOT PEER-REVIEWED | Posted: 10 May 2023 doi:10.20944/preprints202305.0763.v1

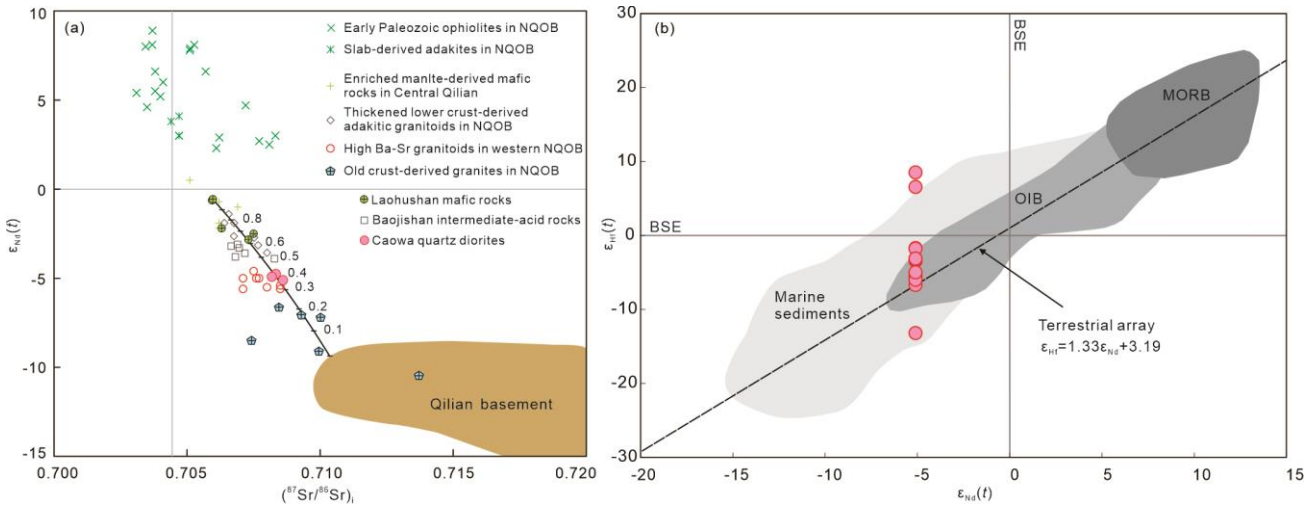

Figure 6. Initial $^{87}Sr/^{86}Sr$ vs. $\varepsilon_{Nd}(t)$ (**a**) and zircon $\varepsilon_{Hf}(t)$ vs. $\varepsilon_{Nd}(t)$ diagrams (**b**) for the Caowa quartz diorites. Data sources: Early Paleozoic ophiolites and slab-derived adakites in the NQOB are from [45–47]; enriched mantle-derived mafic rocks in the Central Qilian are from [70]; thickened lower crust-derived adakitic rocks, high Ba-Sr granitoids and old crust-derived granites in the NQOB are from [10,11,23,58]; Laohushan mafic rocks and Baojishan intermediate-acid rocks in the Eastern NQOB are from [12,59]; Qilian basement from [57]. Fields of MORB, OIB and marine sediments, and Terrestrial array after [71].

4.4. Zircon Hf Isotopes

In situ Hf isotope analyses were carried out on the same zircon domains where the U-Pb dating was done (Figure 3a), and the results of fifty isotopic analyses are listed in Table 4 and shown in Figure 7. The Caowa quartz diorite displays variable $^{176}Hf/^{177}Hf$ ratios (0.282135–0.282753) and $\varepsilon_{Hf}(t)$ values (-13.2 to +8.5), with two-stage Hf model ages (T_{DM}^{c}) of 830–2029 Ma.

Table 4. Zircon Hf isotopic compositions of the Caowa quartz diorites.

Spot No.	Age (Ma)	$^{176}Yb/^{177}Hf$	$^{176}Lu/^{177}Hf$	$^{176}Hf/^{177}Hf$	1σ	$\varepsilon_{Hf}(0)$	$\varepsilon_{Hf}(t)$	T_{DM} (Ma)	T_{DM}^{c} (Ma)	$f_{Lu/Hf}$
CW-6-01	454	0.047583	0.001043	0.282401	0.000028	-13.1	-3.5	1204	1499	-0.97
CW-6-03	442	0.060913	0.001249	0.282459	0.000102	-11.1	-1.7	1128	1393	-0.96
CW-6-04	444	0.053286	0.001496	0.282355	0.000036	-14.7	-5.4	1283	1599	-0.95
CW-6-05	451	0.041103	0.000944	0.282449	0.000048	-11.4	-1.8	1133	1404	-0.97
CW-6-06	457	0.051349	0.001116	0.282409	0.000073	-12.8	-3.1	1195	1483	-0.97
CW-6-07	444	0.074723	0.001580	0.282135	0.000366	-22.5	-13.2	1598	2029	-0.95
CW-6-08	445	0.067271	0.001497	0.282319	0.000104	-16.0	-6.7	1335	1670	-0.95
CW-6-09	441	0.043239	0.001363	0.282365	0.000032	-14.4	-5.1	1264	1578	-0.96
CW-6-10	453	0.053681	0.001471	0.282335	0.000066	-15.4	-5.9	1310	1634	-0.96
CW-6-12	452	0.067973	0.001496	0.282411	0.000057	-12.8	-3.3	1204	1487	-0.95
CW-6-13	448	0.062911	0.001953	0.282340	0.000028	-15.3	-6.0	1320	1634	-0.94
CW-6-14	446	0.079210	0.002148	0.282753	0.000114	-0.7	8.5	730	830	-0.94
CW-6-15	444	0.057545	0.001758	0.282422	0.000041	-12.4	-3.1	1197	1473	-0.95
CW-6-16	449	0.059503	0.001403	0.282364	0.000085	-14.4	-5.0	1268	1579	-0.96
CW-6-19	459	0.061641	0.001196	0.282682	0.000099	-3.2	6.6	812	948	-0.96

Preprints (www.preprints.org) | NOT PEER-REVIEWED | Posted: 10 May 2023 doi:10.20944/preprints202305.0763.v1

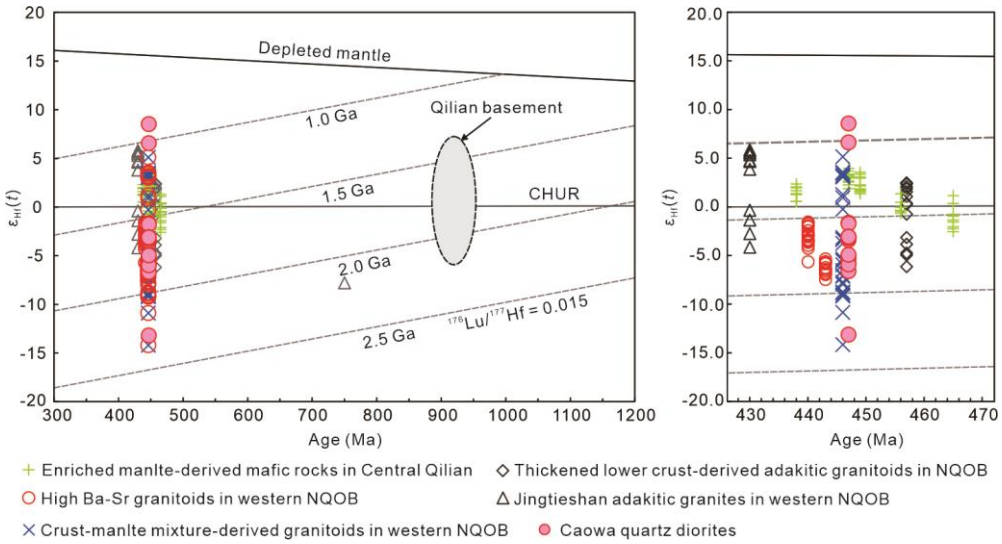

Figure 7. Zircon $\varepsilon_{Hf}(t)$ vs. age (t) diagram for the Caowa quartz diorites. All $\varepsilon_{Hf}(t)$ values were calculated at the ages given by the U–Pb data. Data sources: Jingtieshan adakitic granites and felsic rocks of crust-mantle mixed source in the western part of NQOB are from [72,73]. See Figure 6 for other data sources.

5. Discussion

5.1. Petrogenesis

The whole-rock elemental signatures show that the Caowa quartz diorites are classified as high-K calc-alkaline series. The enrichments in LILEs (e.g. Ba, Th and U) and depletions in HFSEs (e.g. Nb, Ta and Ti), together with the enrichments of LREEs, demonstrate that they are similar to arc magmatic rocks in subduction zones[42]. In addition, the Caowa quartz diorites carry some geochemical characteristics of trace elements that distinguish them from traditional I-, S- and A-type granitoids. On the Rb-Ba-Sr diagram (Figure 8), the samples plot into the field of high Ba–Sr granitoids. The samples show high Ba (822–1165 ppm) and Sr (561–646 ppm) contents and low Rb (72.9–92.1 ppm) and U (1.39–2.17 ppm) contents, together with enrichment in LREEs and depletion in HREEs, and negligible Eu anomalies (Figure 5), which are the typical features for high Ba-Sr granitoids worldwide (e.g., Northern Scotland, Eastern China, ect) [15,17,18,21]. Several models have been proposed for the origin of high Ba-Sr granitoids: (1) partial melting of subducted ocean islands/ocean plateaus [15]; (2) partial melting of thickened mafic lower crust with or without mantle input [19,25,43]; (3) partial melting of enriched lithospheric mantle metasomatized by subduction-related fluids or melts [20,22,23]; (4) mixing of enriched mantle-derived mafic magmas with crustal felsic melts [17,18,26].

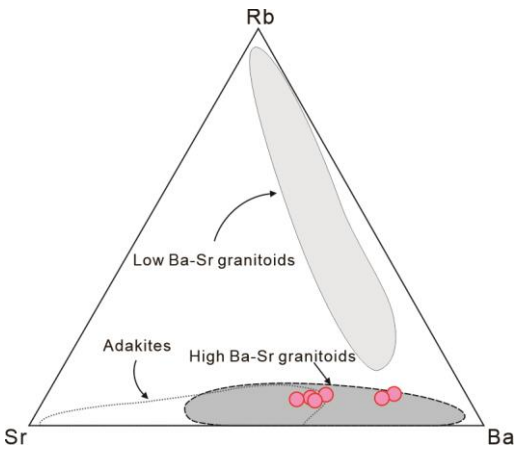

Figure 8. Rb-Ba-Sr ternary diagram for the Caowa quartz diorites, modified after [15].

Preprints (www.preprints.org) | NOT PEER-REVIEWED | Posted: 10 May 2023 doi:10.20944/preprints202305.0763.v1

Tarney and Jones (1994) first proposed that partial melting of subducted oceanic islands or plateaus can generate high Ba-Sr initial magmas, which can also explain their strong fractionated REE patterns and negligible Eu anomalies[15]. However, based on the findings from experimental petrology, partial melting of basaltic oceanic crust (MORB- or OIB) usually produces Na-rich magmas (Na_2O > 5 wt.%)[44], which is evidently inconsistent with the high-K calc-alkaline characteristics of the Caowa quartz diorites (Figure 4b). In addition, the Caowa quartz diorites have enriched Sr-Nd isotope compositons with initial $^{87}Sr/^{86}Sr$ ratios = 0.70818–0.70860 and $\varepsilon_{Nd}(t)$ = -5.1 to -4.9 that are obviously distinct from those of depleted mantle-derived Early Paleozoic ophiolites and adakites in NQOB [45–47] (Figure 6a). Since the partial melting of basaltic oceanic crust cannot generate the Caowa high Ba-Sr quartz diorites.

It is generally accepted that partial melting of thickened mafic lower continental crust is a key mechanism to produce high Ba-Sr granitoids [19,25,43], which is mainly due to their affinities with adakitic granitoids, such as: high alkali, Sr and LREE contents, low Rb, Y and HREE contents, and high Sr/Y and La/Yb ratios [20,48]. Although the rocks studied here display high Sr contents, enrichment in LREE and negligible Eu anomalies (some adakitic features), they have high Y (22.93–33.24 ppm), Yb (2.37–3.17 ppm) contents and low Sr/Y (19–27), La/Yb (4.56–17.47) ratios significantly different to typical adakites (Figure 9), and more evolved Sr-Nd isotope compositons than the adakitic granitoids that are proposed to have been originated from partial melting of thickened lower crust in the eastern part of NQOB [10,11,14] (Figure 6a). Furthermore, magmas, derived from high-pressure partial melting of the thickened lower crust, generally possess extinct fractioned HREE (e.g., Gd/Yb ratios >8) [49]. All samples studied here display low Gd/Yb ratios (1.43–1.72) and flat HREE distribution patterns (Figure 5a), and thus rule out a significant involvement of garnet during the magmatic generation. Consequently, the thickened crust model for the petrogenesis of the high Ba-Sr granitoids is maybe not applicable to the Caowa quartz diorites.

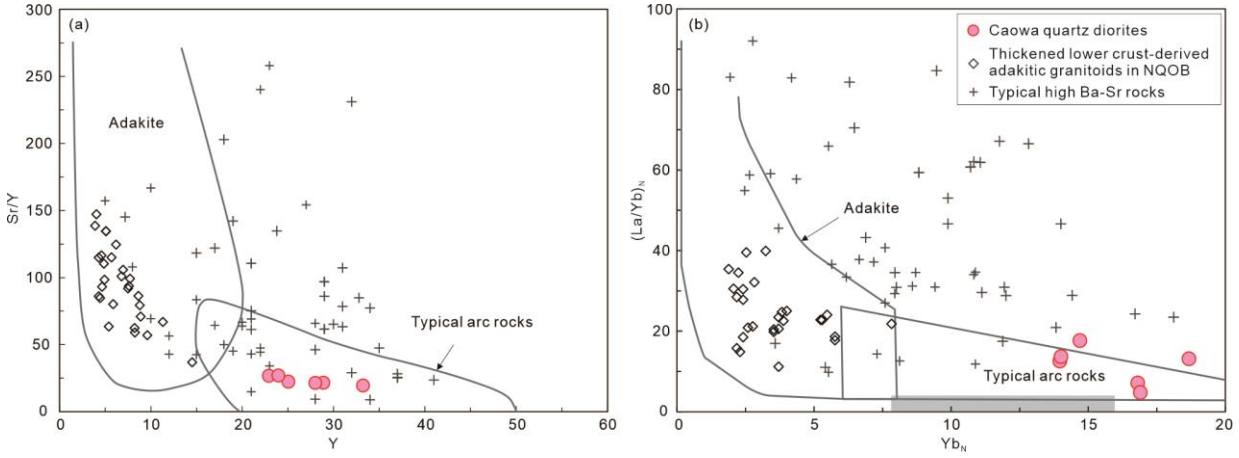

Figure 9. Discrimination diagrams of Sr/Y vs. Y (a) and $(La/Yb)_N$ vs. Yb_N (b) for the Caowa quartz diorites, modified after [48]. See Figure 4 and 6 for the data sources.

Previous studies have shown that subducted oceanic slab and sediments-derived melts or fluids have a high capacity to carry significant amounts of Ba and Sr[50,51], and transfer of these elements would result in enrichment of the overling lithospheric mantle through metasomatism. Thus, low-degree partial melting of enriched lithospheric mantle metasomatized by subduction-related fluids or melts can generate initial magmas with high Ba-Sr signatures[20,22,23]. The Caowa quartz diorites exhibit higher Nd (21.20–45.27 ppm), Nb (12.20–13.84 ppm) contents and Nb/Ta (14.46–20.22) values than those derived from the continent crust (Nd = 11–27, average Nb/Ta = 11)[52], indicating the significant contribution of mantle components. Besides, the Caowa quartz diorites have relatively enriched Sr-Nd-Hf isotopic compositions, which are consistent with those of the enriched

 doi:10.20944/preprints202305.0763.v1

mantle-derived high Ba-Sr granitoids from the southern margin of Alxa block (Figure 6a, Figure 7)[23]. As shown in plots of Ba/Th vs. Th/Zr and Rb/Y vs. Nb/Y (Figure 10), magma sources for the Caowa quartz diorites were probably related to the lithospheric mantle metasomatized by subduction-related fluids. This is also confirmed by the Nd-Hf isotope decoupling (Figure 6b), owing to the discrepant elemental behavior between Nd and Hf. Normally, Nd is much more mobile than Hf in subduction zone, it is difficult to cause Hf isotope enrichment when metasomatism occurs with the overlying lithospheric mantle[53,54], which is consistent with the occurrence of positive $\varepsilon_{Hf}(t)$ values for the Caowa dioritic intrusion (e.g., +6.6 and +8.5). However, it should be noted that partial melting of enriched mantle model provides a certain degree of support for the high Ba-Sr signatures of Caowa quartz diorites, but the relatively low MgO (2.08–3.01 wt.%), $Mg^{\#}$ (42–44), Cr (4.58–6.43 ppm) and Ni (3.29–5.12 ppm) contents of these rocks are distinct from the high-Mg diorites and clearly argue against a single, common mantle evolution by partial melting process[55,56]. Since, such mechanism is not feasible here, we interpret that the magma source of these rocks may also have the addition of continental crustal components.

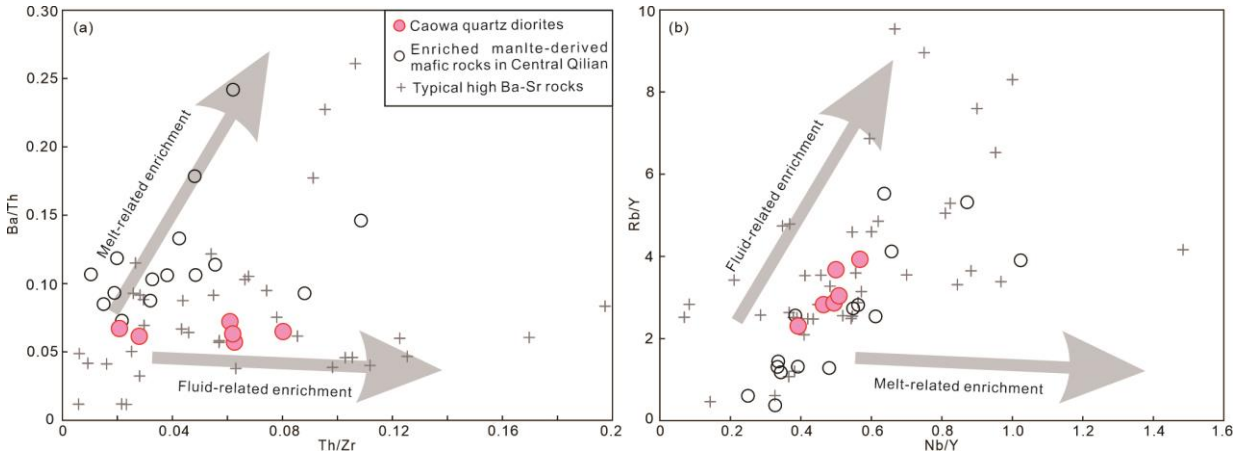

Figure 10. Ba/Th vs. Th/Zr(a) and Rb/Yb vs. Nb/Yb (b) diagrams for the Caowa quartz diorites, modified after [22]. See Figure 4 and 6 for the data sources.

Here, we propose that the studied Caowa high Ba-Sr quartz diorites probably generated through mixing of enriched lithospheric mantle-derived basaltic and crustal felsic magmas. Their moderate SiO_2 (57.53–62.87 wt.%), MgO (2.08–3.01 wt.%) contents and $Mg^{\#}$ values (42–44), as well as the wide ranges of zircon Hf isotopes, support the mechanism of crust-mantle interaction (Figure 7). The studied rocks exhibit more radiogenic Sr and Nd isotopes when compared to the enriched mantle-derived mafic rocks from Central and North Qilian, and which are also different from those of the Precambrian metamorphic basement and associated granites (Figure 6a)[57,58]. A simple isotope model was adopted to evaluate the possible mixing proportion of mantle and crustal components, it is suggested that the Caowa high Ba-Sr quartz diorites might be products of mixing of 40% enriched mantle and 60% ancient crustal melts (Figure 6a). Besides, the Caowa quartz diorites are associated with the contemporary mafic rocks, dioritic enclaves, and felsic rocks in the surrounding areas, Such as Laohushan-Quwushan Mountain (Figure 1b), which were considered to be derived from partial melting of the metasomatized enriched lithosphere mantle, magma mixing, and partial melting of lower continental crust, respectively [11,13,59,60]. Successive variation in major elemental compositions between them (Figure 11), further substantiates a petrogenetic model of crust-mantle interaction [61,62]. Such a crust-mantle interaction mechanism can be further testified by the hyperbolic curves in diagrams involving the incompatible elements and its ratios [61,63]. In the Th vs. Th/Nd and Th/La vs. Zr/Sm diagrams, the studied rocks and associated contemporary mafic rocks, dioritic enclaves, and felsic rocks in the surrounding areas composed a

Preprints (www.preprints.org) | NOT PEER-REVIEWED | Posted: 10 May 2023 doi:10.20944/preprints202305.0763.v1

characteristic hyperbolic mixing line (Figure 12), which confirms the major role of two-component mixing process. In order to further evaluate the possibility of magma mixing, both Laohushan hornblendite xenoliths (represented by enriched mantle source) and Quwushan granodiorites (represented by lower crustal source) were chosen as mixing end-members in the geochemical simulation. The modeling results show that the Caowa high Ba-Sr quartz diorites accords with formation of crustal and mantle melts mixing and the mixture proportion was approximately 6:4 (Figure 12b), which was consistent with the Sr-Nd isotope simulation results (Figure 6a).

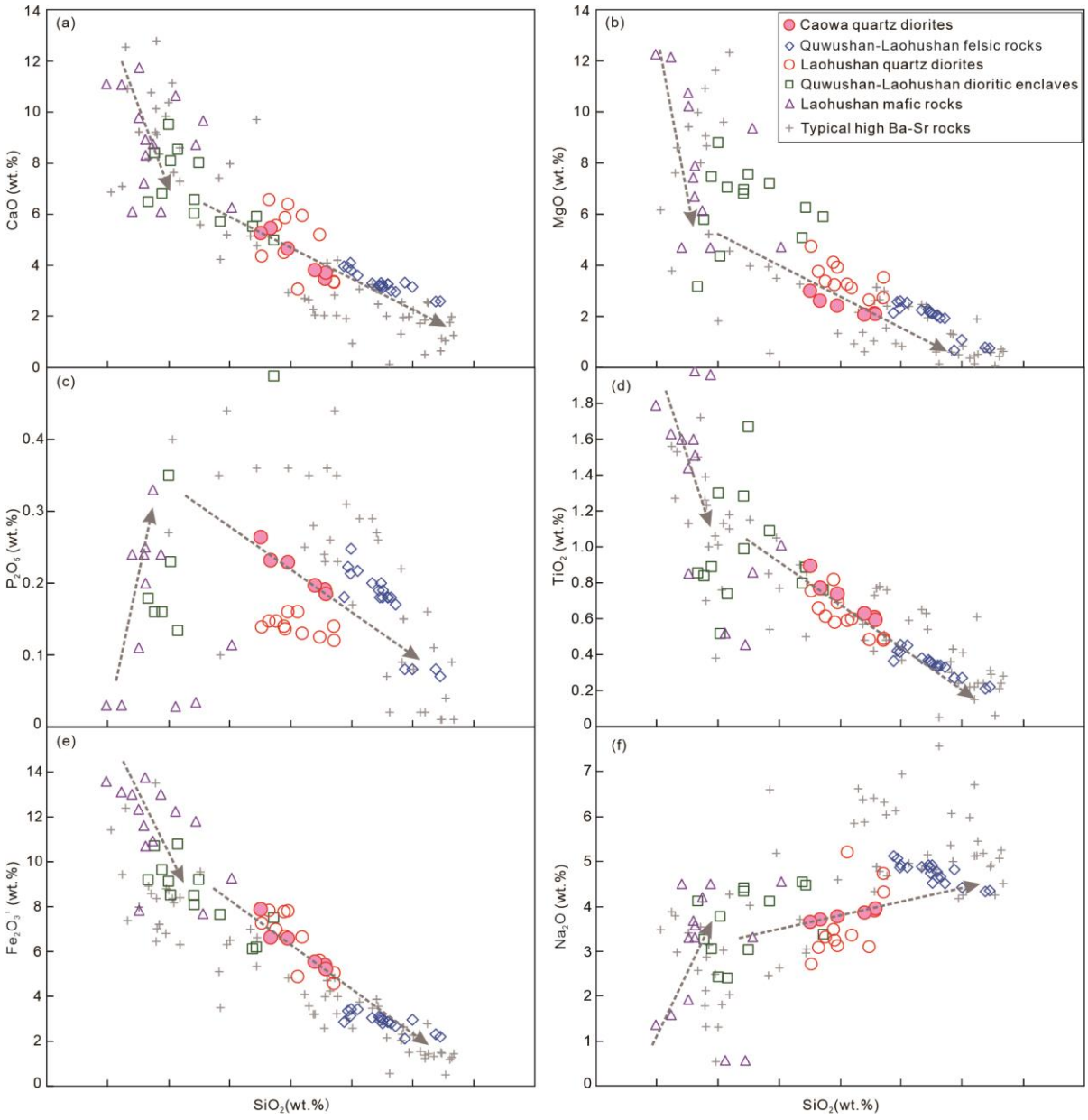

Figure 11. Hark diagrams for the Caowa quartz diorites. Data sources: Quwushan-Laohushan mafic rocks, dioritic enclaves and intermediate-acid rocks are from [13,59,60]. See Figure 4 for other data sources.

 doi:10.20944/preprints202305.0763.v1

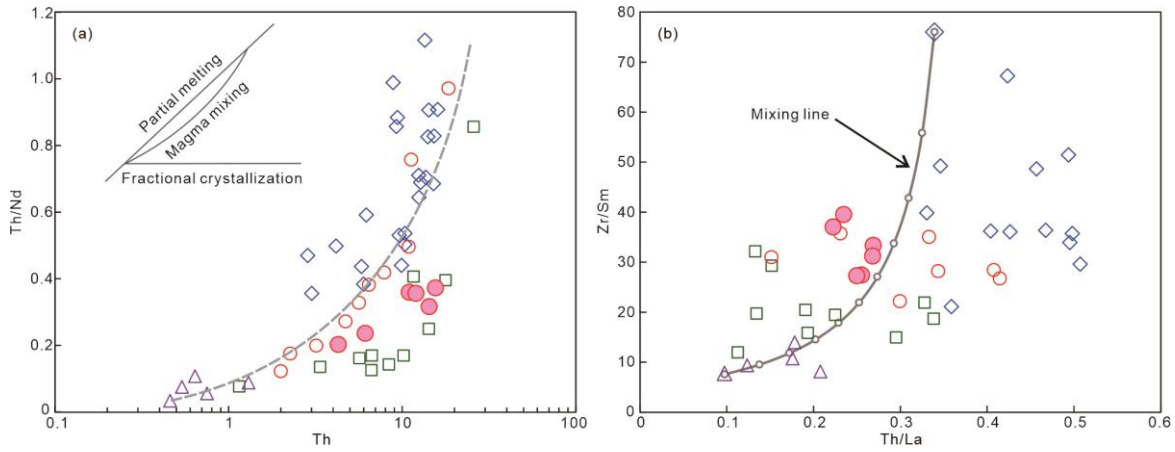

Figure 12. Th/Nd vs. Th (**a**) and Zr/Sm vs. Th/La (**b**) diagrams for the Caowa quartz diorites, modified after [63]. See Figure 11 for the symbols and data sources.

In summary, the petrogenesis of Caowa high Ba-Sr intrusion can be explained by a two-stage model: firstly, a low-degree partial melting of enriched lithospheric mantle metasomatized by subduction-related fluids generated initial magmas with high Ba-Sr signatures, and then underplating of this high Ba-Sr basaltic melts triggered partial melting of the ancient lower continental crust and subsequent crust-mantle interaction.

5.2. Tectonic Implications

It is generally accepted that the Early Paleozoic NQOB is a typical subduction-accretionary orogenic belt, marking the tectonic evolution of Proto-Tethys Ocean [1,2,9,27]. Although both the Proto-Tethys Ocean subduction-related and the syn-collision/post-collision tectonic settings have been proposed, the subduction polarity and final closure of the Proto-Tethys Ocean are still controversial. The models of the subduction polarity issue include southward subduction [64], northward subduction [5,8,9], or bidirectional subduction [32,65]. However, considering the current tectonic geographical pattern and the distribution of Early Paleozoic mid-ocean-ridge type ophiolites, high-pressure metamorphic rocks, arc magmatic rocks and back-arc basin ophiolites in the NQOB from south to north, northward subduction of the Qilian Proto-Tethys ocean was basically authenticated, and the closure time of the Qilian Proto-Tethys ocean was no later than 440 Ma [5,7–9]. It should be noted that these previous studies concerning the Proto-Tethys evolution have focused on the western part of the NQOB. As for the eastern part of the NQOB, the former evolution process may be suffered "acclimatized" [14].

Yu et al. (2015) believed that the generation of crustal-derived low-Mg adakitic granitoids (461–440 Ma) from the Eastern NQOB reflects crustal thickening in response to an continent-continent collision [11]. As mentioned above, the Caowa high Ba-Sr dioritic intrusion examined in the Nanhuashan area of the Eastern NQOB was not correlate with crustal thickening which should display high Gd/Yb ratios and leave a residue with garnet. In addition, the distributions of the ca. 448 Ma Laohushan ophiolite (the Northern ophiolite belt, Figure 1b) and ca. 446 Ma Baiyin arc volcanic rocks indicate that the Eastern NQOB was probably undergone a new oceanic crust development and subduction during the Late Ordovician [5,8,59]. Combined with the new discovery of boninitic blueschists and associated greenschists from Laohushan area in Eastern NQOB by Fu et al. (2022) [29], which record the intra-oceanic subduction initiation at ca. 492–488 Ma, we assume that there may be no continent-continent event occurring there before Late Ordovician.

The Late Ordovician Caowa high-Ba-Sr quartz diorites studied here are located in the eastern part of the NQOB (Figure 1). As discussed above, these rocks generated through interaction of partial melts derived from subduction-related metasomatized lithospheric mantle and ancient lower continental crust. Therefore, we propose that they are most probably formed in a Late Ordovician oceanic crust subduction-related arc setting. The

Preprints (www.preprints.org) | NOT PEER-REVIEWED | Posted: 10 May 2023 doi:10.20944/preprints202305.0763.v1

distribution of these rocks occurring to the northeast of Baiyin arc and Laohushan ophiolite belt and the southern margin of Alxa block (Figure 1b) indicates that they were related to the northward subduction of the North Qilian oceanic crust formed in a back-arc basin rather than the paleo-Qilian ocean (maybe a main ocean of Proto-Tethys in the Qilian orogenic system). Consequently, we suggest that affected by the northward subduction of the Qilian Proto-Tethys ocean, the Laohushan oceanic crust of the North Qilian back-arc basin was subducted during the Late Ordovician, which induced extensive metasomatism of lithospheric mantle by subduction-related fluids and subsequent crust-mantle interaction during the Late Ordovician (Figure 13).

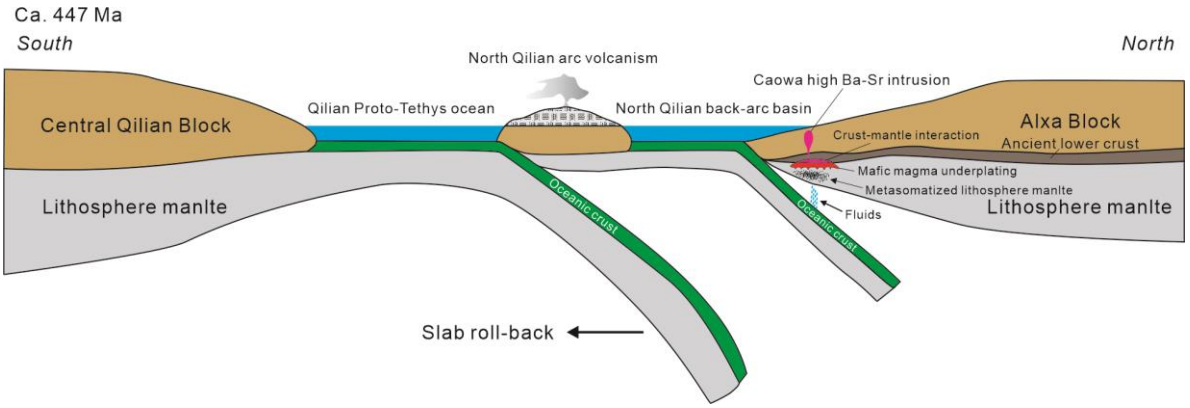

Figure 13. Schematic diagram of the possible tectonic setting and petrogenesis of the Caowa high Ba-Sr dioritic intrusion, and the Late Ordovician tectonic evolution of the NQOB.

6. Conclusions

(1) Zircon U-Pb dating suggests that the Caowa dioritic intrusion from Nanhuashan area have magma crystallization age of 447 Ma, representing Late Ordovician magmatism in the eastern part of North Qilian orogenic belt.

(2) The petrographic, geochemical and Sr-Nd-Hf isotopic characteristics indicate that the Caowa quartz diorites, classified as high Ba-Sr granitoids, were produced through a crust-mantle interaction between partial melt derived from subduction-related fluids metasomatized lithospheric mantle and ancient lower crust-derived magma.

(3) The petrogenesis of the Caowa high Ba-Sr dioritic intrusion in Nanhuashan area provides support for an existence of northward subduction of the North Qilian oceanic crust (Laohushan back-arc oceanic basin) in the eastern part of the North Qilian orogenic belt during the Late Ordovician.

Author Contributions: Conceptualization, S.Z. and L.H.; methodology, B.L.; software, H.D. and Q.X.; formal analysis, S.Z.; investigation, S.Z., L.H. and C.M.; resources, X.W. and C.X.M.; writing-original draft preparation, S.Z.; writing-review and editing, L.H. and B.L.; project administration, L.H. and X.W.; funding acquisition, B.L., H.D. and C.X.M. All authors have read and agreed to the published version of the manuscript.

Funding: This study is co-supported by the National Natural Science Foundation of China (Grant No. 42130309, 41802085), the Provincial Key Research & Development Program of Ningxia Hui Autonomous Region (Grant No. 2021BEG03003), and the Provincial Natural Science Foundation of Ningxia Hui Autonomous Region (Grant No. 2021AAC03447).

Data Availability Statement: The original contributions presented in the study are included in the article.

Acknowledgments: We thank Jinwei Guo for scientific discussions which are helpful for this manuscript.

Conflicts of Interest: The authors declare no conflict of interest.

References

1. Zhang, J.X.; Yu, S.Y.; Li, Y.S.; Yu, X.X.; Lin, Y.H.; Mao, X.H. Subduction, accretion and closure of Proto-Tethyan Ocean: Early Paleozoic accretion/collision orogeny in the Altun-Qilian-North Qaidam orogenic system. *Acta Petrol. Sin.* 2015, 31, 3531-3554, (in Chinese with English abstract).
2. Yu, S.Y.; Peng, Y.B.; Zhang, J.X.; Li, S.Z.; Santosh, M.; Li, Y.S.; Liu, Y.J.; Gao, X.Y.; Ji, W.T.; Lv, P.; Li, C.Z.; Jiang, X.Z.; Qi, L.L.; Xie, W.M.; Xu, L.J. Tectono-thermal evolution of the Qilian orogenic system: Tracing the subduction, accretion and closure of the Proto-Tethys Ocean. *Earth Sci. Rev.* 2021, 215, 103547.
3. Xiao, W.J.; Windley, B.F.; Yong, Y.; Yan, Z.; Yuan, C.; Liu, C.Z.; Li, J.L. Early Paleozoic to Devonian multiple-accretionary model for the Qilian Shan, NW China. *J. Asian Earth Sci.* 2009, 35, 323-333.
4. Xu, Z.Q.; Xu, H.F.; Zhang, J.X.; Li, H.B.; Zhu, Z.Z.; Qu, J.C.; Chen, D.Z.; Chen, J.L.; Yang, K.C. The Zhoulangnanshan Caledonian subductive complex in the Northern Qilian Mountains and its dynamics. *Acta Geol. Sin.* 1994, 68, 1-15, (in Chinese with English abstract).
5. Song, S.G; Niu, Y.L.; Su, L.; Xia, X.H. Tectonics of the North Qilian orogen, NW China. *Gondwana Res.* 2013, 23, 1378-1401.
6. Xia, L,Q.; Li, X.M.; Yu, J.Y.; Wang, G.Q. Mid-Late Neoproterozoic to Early Paleozoic volcanism and tectonic evolution of the Qilian Mountain. *China Geology*, 2016, 43, 1087-1138 (in Chinese with English abstract).
7. Wu, C.L.; Xu, X.Y.; Gao, Q.M.; Li, X.M.; LeI, Min.; Gao, Y.H.; Frost, R.B.; Wooden, J.L. Early Palaezoic granitoid magmatism and tectonic evolution in North Qilian, NW China. *Acta Petrol. Sin.* 2010, 26, 1027-1044 (in Chinese with English abstract).
8. Wang, C.Y.; Zhang, Q.; Qian, Q.; Zhou, M.F. Geochemistry of the Early Paleozoic Baiyin Volcanic Rocks (NW China): Implications for the Tectonic Evolution of the North Qilian Orogenic Belt. *J. Geol.* 2005, 113, 83-94.
9. Xia, L.Q.; Li, X.M.; Yu, J.Y.; Wang, G.Q. Mid-late neoproterozoic to early paleozoic volcanism and tectonic evolution of the Qilianshan, NW China. *GeoResJ*, 2016, 9-12, 1-41.
10. Tseng, C.Y.; Yang, H.J.; Yang, H.Y.; Liu, D.Y.; Wu, C.L.; Cheng, C.K.; Chen, C.H.; Ker, C.M. Continuity of the North Qilian and North Qinling orogenic belts, Central Orogenic System of China: Evidence from newly discovered Paleozoic adakitic rocks. *Gondwana Res.* 2009, 16, 285-293.
11. Yu, S.Y.; Zhang, J.X.; Qin, H.P.; Sun, D.Y.; Zhao, X.L.; Cong, F.; Li, Y.S. Petrogenesis of the early Paleozoic low-Mg and high-Mg adakitic rocks in the North Qilian orogenic belt, NW China: Implications for transition from crustal thickening to extension thinning. *J. Asian Earth Sci.* 2015, 107, 122-139.
12. Chen, S.; Niu, Y.L.; Sun, W.L.; Zhang, Y.; Li, J.Y.; Guo, P.Y.; Sun, P. On the origin of mafic magmatic enclaves (MMEs) in syn-collisional granitoids: evidence from the Baojishan pluton in the North Qilian Orogen, China. *Miner Petrol*, 2015, 109, 577-596.
13. Chen, S.; Niu, Y.L.; Li, J.Y.; Sun, W.L.; Zhang, Y.; Hu, Y.; Shao, F.L. Syn-collisional adakitic granodiorites formed by fractional crystallization: Insights from their enclosed mafic magmatic enclaves (MMEs) in the Qumushan pluton, North Qilian Orogen at the northern margin of the Tibetan Plateau. *Lithos*, 2016, 248-251, 455-468.
14. Yang, H.; Zhang, H.F.; Xiao, W.J.; Zhang, J.; Xiong, Z.L.; Guo, L.; Pan, F.B. Petrogenesis of Early Paleozoic high Sr/Y intrusive rocks from the North Qilian orogen: Implication for diachronous continental collision. *Lithosphere*, 2019, 12, 53-73.
15. Tarney, J.; Jones, C.E. Trace element geochemistry of orogenic igneous rocks and crustal growth models. *J. Geol. Soc.* 1994, 151, 855-868.
16. Fowler, M.B.; Henney, P.J.; Darbyshire, D.P.F.; Greenwood, P.B. Petrogenesis of high Ba-Sr granites; the Rogart Pluton, Sutherland. *J. Geol. Soc.* 2001, 158, 521-534.
17. Qian, Q.; Chung, S.L.; Lee, T.Y.; Wen, D.J. Mesozoic high-Ba-Sr granitoids from North China: geochemical characteristics and geological implications. *Terra Nova*, 2003, 15, 272-278.
18. Wang, Z.L.; Zhao, R.X.; Zhang, Q.; Lu, H.W.; Li, J.L.; Cheng, W. Magma mixing for the high Ba-Sr Guojialing-type granitoids in Northwest Jiaodong Peninsula: Constraints from petrogeochemistry and Sr-Nd isotopes. *Acta Petrol. Sin.* 2014, 30, 2595-2608 (in Chinese with English abstract).
19. Choi, S.G.; Rajesh, V.J.; Seo, J.; Park, J.W.; Oh, C.W.; Pak, S.J.; Kim, S.W. Petrology, geochronology and tectonic implications of Mesozoic high Ba-Sr granites in the Haemi area, Hongseong Belt, South Korea. *Island Arc*, 2009, 18, 266-281.
20. Fowler, M.B.; Kocks, H.; Darbyshire, D.P.F.; Greenwood, P.B. Petrogenesis of high Ba–Sr plutons from the Northern Highlands Terrane of the British Caledonian Province. *Lithos*, 2008, 105, 129-148.
21. Peng, T.P.; Wilde, S.A.; Fan, W.M.; Peng, B.X. Late Neoarchean potassic high Ba–Sr granites in the Taishan granite–greenstone terrane: Petrogenesis and implications for continental crustal evolution. *Chem. Geol.* 2013, 344, 23-41.
22. Ren, L.; Liang, H.Y.; Bao, Z.W.; Zhang, J.; Li, K.X.; Huang, W.T. The petrogenesis of early Paleozoic high-Ba–Sr intrusions in the North Qinling terrane, China, and tectonic implications. *Lithos*, 2018, 314-315, 534-550.
23. Zhang, L.Q.; Zhang, H.F.; Hawkesworth, C.; Luo, B.J.; Yang, H.; Xu, W.C.; Guo, L.; Pan, F.B.; Gao, Z.; Tao, L. Sediment contribution in post-collisional high Ba-Sr magmatism: Evidence from the Xijing pluton in the Alxa block, NW China. *Gondwana Res.* 2019, 69, 177-192.
24. Wang, Y.F.; Shao, Y.; Jiang, S.Y.; Zhang, Z.Z.; Hu, J.; Xiao, E.; Dai, B.Z.; Li, H.Y. Petrogenesis of Indosinian High Ba-Sr Granites in Laoniushan Batholith, Shaanxi Province and Their Tectonic Implications. *Geo. J. China Univ.* 2012, 18, 133-149 (in Chinese with English abstract).

25. Ye, H.M.; Li, X.H.; Li, Z.X.; Zhang, C.L.; Age and origin of high Ba–Sr appinite–granites at the northwestern margin of the Tibet Plateau: Implications for early Paleozoic tectonic evolution of the Western Kunlun orogenic belt. *Gondwana Res.* 2008, 13, 126-138.
26. Zhang, Y.Y.; Sun, M.; Yuan, C.; Xu, Y.G.; Long, X.P.; Magma mixing origin for high Ba–Sr granitic pluton in the Bayankhongor area, central Mongolia: Response to slab roll-back. *J. Asian Earth Sci.* 2015, 113, 353-368.
27. Song, S.G.; Wu, Z.Z.; Yang, L.M.; Su, L.; Xia, X.H.; Wang, C.; Dong, J.L.; Zhou, C.A.; Bi, H.Z. Ophiolite belts and evolution of the Proto-Tethys Ocean in the Qilian Orogen. *Acta Petrol. Sin.* 2019, 35, 2948-2970 (in Chinese with English abstract).
28. Qian, Q.; Zhang, Q.; Sun, X.M.; Wang, Y.M. Geochemical features and tectonic setting for basalts and cherts from Laohushan, North Qilian. *Sci Geol. Sin.* 2001, 36, 444-453 (in Chinese with English abstract).
29. Fu, D.; Huang, B.; Johnson, T.E.; Wilde, S.A.; Jourdan, F.; Polat, A.; Windley, B.F.; Hu, Z.C.; Kusky, T. Boninitic blueschists record subduction initiation and subsequent accretion of an arc–forearc in the northeast Proto-Tethys Ocean. *Geology*, 2022, 50, 10-15.
30. Zhang, J.X.; Meng, F.C.; Wan, Y.S. A cold early Palaeozoic subduction zone in the North Qilian Mountains, NW China: petrological and U-Pb geochronological constraints. *J. Meta Geol.* 2007, 25, 285-304.
31. Song, S.G.; Niu, Y.L.; Zhang, L.F.; Wei, C.J.; Liou, J.G.; Su, L. Tectonic evolution of early Paleozoic HP metamorphic rocks in the North Qilian Mountains, NW China: New perspectives. *J. Asian Earth Sci.* 2009, 35, 334-353.
32. Wu, C.L.; Gao, Y.H.; Frost, B.R.; Robison, P.T.; Wooden, J.L.; Wu, S.P.; Chen, Q.L.; Lei, M. An early Palaeozoic double-subduction model for the North Qilian oceanic plate: evidence from zircon SHRIMP dating of granites. *Int. Geol. Rev.* 2011, 53, 157-181.
33. Wang, J.R.; Wu, C.J.; Cai, Z.H.; Guo, Y.S.; Wu, J.C.; Liu, X.H. Early Paleozoic high-Mg adakite from Yindongliang in the eastern section of the North Qilian: Implications for geodynamics and Cu-Au mineralization. *Acta Petrol. Sin.* 2006, 22, 2655-2664 (in Chinese with English abstract).
34. Hu, Z.C.; Zhang, W.; Liu, Y.S.; Gao, S.; Li, M.; Zong, K.Q.; Chen, H.H.; Hu, S.H. "Wave" signal-smoothing and mercury-removing device for laser ablation quadrupole and multiple collector ICPMS analysis: application to lead isotope analysis. *Anal. Chem.* 2015, 87, 1152-1157.
35. Zong, K.Q.; Klemd, R.; Yuan, Y.; He, Z.Y.; Guo, J.L.; Shi, X.L.; Liu, Y.S.; Hu, Z.C.; Zhang, Z.M. The assembly of Rodinia: The correlation of early Neoproterozoic (ca. 900 Ma) high-grade metamorphism and continental arc formation in the southern Beishan Orogen, southern Central Asian Orogenic Belt (CAOB). *Precambrian Res*. 2017, 290, 32-48.
36. Liu, Y.S.; Gao, S.; Hu, Z.C.; Gao, C.G.; Zong, K.Q.; Wang, D.B. Continental and Oceanic Crust Recycling-induced Melt-peridotite Interactions in the Trans-North China Orogen: U-Pb Dating, Hf Isotopes and Trace Elements in Zircons of Mantle Xenoliths. *J. Petrol.* 2010, 51, 537-571.
37. Ludwig, K.R. *User's Manual for Isoplot/ex Version 3.00: A Geochronological Toolkit for Microsoft Excel*; Special Publication; Berkeley Geochronology Center: Berkeley, CA, USA, 2003.
38. Hu, Z.C.; Liu, Y.S.; Gao, S.; Liu, W.G.; Zhang, W.; Tong, X.R.; Lin, L.; Zong, K.Q.; Li, M.; Chen, H.H.; Zhou, L.; Yang, L. Improved in situ Hf isotope ratio analysis of zircon using newly designed X skimmer cone and Jet sample cone in combination with the addition of nitrogen by laser ablation multiple collector ICP-MS. *J. Anal. At. Spectrom.* 2012, 27, 1391-1399.
39. Zhang, W.; Hu, Z.C.; Spectroscopy, A. Estimation of Isotopic Reference Values for Pure Materials and Geological Reference Materials. *Atom. Spectrosc.* 2020, 41, 93-102.
40. Griffin, W.L.; Belousova, E.A.; Shee, S.R.; Pearson, N.J.; O'Reilly, S.Y. Archean Crustal Evolution in the Northern Yilgarn Craton: U-Pb and Hf-isotope Evidence from Detrital Zircons. *Precambrian Res.* 2004, 131, 231-282.
41. Paul, W. O. H,; Urs, S. The Composition of Zircon and Igneous and Metamorphic Petrogenesis. *Rev. Mineral. Geochem.* 2003, 53, 27-62.
42. Kelemen, P.B.; Hanghøj, K.; Greene, A.R. One View of the Geochemistry of Subduction-Related Magmatic Arcs, with an Emphasis on Primitive Andesite and Lower Crust. *Treatise. Geochem.* 2003. 3: p. 593-659.
43. Yang, L.Q.; Dilek, Y.; Wang, Z.L.; Weinberg, R.F.; Liu, Y. Late Jurassic, high Ba–Sr Linglong granites in the Jiaodong Peninsula, East China: lower crustal melting products in the eastern North China Craton. *Geol. Mag*. 2018, 155, 1040-1062.
44. Beard, J.S.; Lofgren, G.E. Dehydration Melting and Water-Saturated Melting of Basaltic and Andesitic Greenstones and Amphibolites at 1, 3, and 6.9 kb. *J. Petrol.* 1991, 32, 365-401.
45. Qian, Q.; Zhang, Q. Geochemical characteristics and tectonic setting of the Laohushan Basalts, north Qilian Mountains. *Acta Geol. Sin.* 2001, 75, 452-457.
46. Hou, Q.Y.; Zhao, Z.D.; Zhang, B.R.; Zhang, H.F.; Zhang, L.; Chen, Y.L. On the boundary of Tethyan tectonic domain on northeastern margin of the Tibetan Plateau. *Acta Petrol. Sin.* 2006, 22, 567-577 (in Chinese with English abstract).
47. Chen, Y.X.; Xia, X.H.; Song, S.G. Petrogenesis of Aoyougou high-silica adakite in the North Qilian orogen, NW China: Evidence for decompression melting of oceanic slab. *Chin. Sci. Bull.* 2012, 57, 2072-2085 (in Chinese with English abstract).
48. Martin, H.; Smithies, R.H.; Rapp, R.; Moyen, J.F.; Champion, D. An overview of adakite, tonalite–trondhjemite–granodiorite (TTG), and sanukitoid: relationships and some implications for crustal evolution. *Lithos*, 2005, 79, 1-24.
49. Qian, Q.; Hermann, J. Partial melting of lower crust at 10–15 kbar: constraints on adakite and TTG formation. *Contrib. Mineral. Petrol.* 2013, 165, 1195-1224.
50. Vigouroux, N.; Wallace, P.J.; Kent, A.J.R. Volatiles in High-K Magmas from the Western Trans-Mexican Volcanic Belt: evidence for Fluid Fluxing and Extreme Enrichment of the Mantle Wedge by Subduction Processes. *J. Petrol.* 2008, 49, 1589-1618.

51. Hermann, j.; Rubatto, D. Accessory phase control on the trace element signature of sediment melts in subduction zones. *Chem. Geol.* 2009, 265, 512-526.
52. Sun, S.S.; McDonough, W.F. Chemical and isotopic systematics of oceanic basalts:implications for mantle composition and processes. In *Magmatism in the Ocean Basins*; Saunders, A.D., Norry, M.J., Eds.; Special Publications; Geological Society: London, UK, 1989, 42, 313–345.
53. Vervoort, J.D.; Patchett, P.J.; Blichert-Toft, J.; Albarède F. Relationships between Lu-Hf and Sm-Nd Isotopic Systems in the Global Sedimentary System. *Earth Planet. Sci. Lett.* 1999, 168, 79-99.
54. Hoffmann, J.E., Münker, C., Polat, A. Rosing, M.T.; Schulz, T. The Origin of Decoupled Hf-Nd Isotope Compositions in Eoarchean Rocks from Southern West Greenland. *Geochim. Cosmochim. Acta*. 2011, 75, 6610-6628.
55. Tan, J.; Wei, J.H.; Zhao, S.Q.; Li, Y.J.; Liu, Y.; Liu, X.Y.; Zhang, F.; Ga, J.R.; Wang, Z.H. Petrogenesis of Late Triassic high-Mg diorites and associated granitoids with implications for Paleo-Tethys evolution in the northeast Tibetan Plateau. *Geol. Soc. Am. Bull.* 2019, 132, 955-976.
56. Zhao, S.Q.; Fu, L.B.; Wei, J.H.; Tan, J.; Wang, X.C.; Zhao, Z.X.; Li, X. Petrogenesis and Geodynamic Setting of Late Triassic Quartz Diorites in Zhiduo Area, Qinghai Province. *Earth Sci.* 2015, 23, 185-220 (in Chinese with English abstract).
57. Tao, L.; Zhang, H.F.; Gao, Z.; Yang, H.; Zhang, L.Q.; Guo, L.; Pan, F.B. Across-arc geochemical and Sr–Nd–Hf isotopic variations of mafic intrusive rocks at the southern Central Qilian block, China. *Gondwana Res.* 2018, 59, 108-125.
58. Wang, K.X.; Yu, C.D.; Yan, J.; Liu, X.D.; Liu, W.H.; Pan, J.Y. Petrogenesis of Early Silurian granitoids in the Longshoushan area and their implications for the extensional environment of the North Qilian Orogenic Belt, China. *Lithos*, 2019, 342-343, 152-174.
59. Fu, D.; Kusky, T.; Wilde, S.A.; Polat, A.; Huang, B.; Zhou, Z.P. Early Paleozoic collision-related magmatism in the eastern North Qilian orogen, northern Tibet: A linkage between accretionary and collisional orogenesis. *Geol. Soc. Am. Bull.* 2018, 131, 1031-1056.
60. Chen, S.; Niu, Y.L.; Xue, Q.Q. Syn-collisional felsic magmatism and continental crust growth: A case study from the North Qilian Orogenic Belt at the northern margin of the Tibetan Plateau. *Lithos*, 2018, 308-309, 53-64.
61. Langmuir, C.H.; Vocke, R.D.; Hanson, G.N.; Hart, S.R. A general mixing equation with applications to Icelandic basalts. *Earth Planet. Sci. Lett.* 1978, 37, 380-392.
62. Lee, C-T.A.; Bachmann, O. How important is the role of crystal fractionation in making intermediate magmas? Insights from Zr and P systematics. *Earth Planet. Sci. Lett.* 2014, 393, 266-274.
63. Schiano, P.; Monzier, M.; Eissen, J.P.; Martin, H.; Koga, K.T. Simple mixing as the major control of the evolution of volcanic suites in the Ecuadorian Andes. *Contrib. Mineral. Petrol.* 2010, 160, 297-312.
64. Peng, Y.B.; Yu, S.Y.; Zhang, J.X.; Li, S.Z.; Tong, L.X.; Sun, D.Y. Early Paleozoic arc magmatism and metamorphism in the northern Qilian Block, western China: Petrological and geochronological constraints. *Geol. J.* 2017, 52, 339-364.
65. Zhang, J.X.; Li, J.P.; Yu, S.Y.; Meng, F.C.; Mattinson, C.G.; Yang, H.J.; Ker, C.M. Provenance of eclogitic metasediments in the north Qilian HP/LT metamorphic terrane, western China; geodynamic implications for early Paleozoic subduction-erosion. *Tectonophysics*, 2012, 570-571, 78-101.
66. Wilson, M. *Igneous petrogenesis*. Unwim Hyman, London, 1989, 1-366.
67. Rollinson, H.R. *Using Geochemical Data: Evaluation, Presentation, Interpretation*. Longman Group UK Ltd, New York, 1993, 1-352.
68. Frost, B.R.; Barnes, C.G.; Collins, W.J.; Arculus, R.J. A geochemical classification for granitic rocks. *J. Petrol.* 2001, 42, 2033-2048.
69. Maniar, P.D.; Piccoli, P.M. Tectonic Discrimination of Granitoids. *Geol. Soc. Am. Bull.* 1989, 101, 635-643.
70. Yang, H.; Zhang, H.F.; Luo, B.J; Zhang, J.; Xiong, Z.L.; Guo, L.; Pan, F.B. Early Paleozoic intrusive rocks from the eastern Qilian orogen, NE Tibetan Plateau: Petrogenesis and tectonic significance. *Lithos*, 2015, 224-225, 13-31.
71. Vervoort, J.D.; Plank, T.; Prytulak, J. The Hf–Nd isotopic composition of marine sediments. *Cosmochim. Acta*. 2011, 75, 5903-5926.
72. Li, Y.S.; Xu, L.J.; Yu, S.Y.; Zhang, J.X.; Guo, J.; Peng, Y.B.; Zhou, G.S. Partial melting of thickened lower crust in post-collisional setting: Evidence from high silicon adakitic granites in the North Qilian orogen. *Geol. J.* 2020, 55, 3990-4007.
73. Wang, C.; Li, R.S.; Smithies, R.H.; Li, M.; Peng, Y.; Chen, F.N.; He, S.P. Early Paleozoic felsic magmatic evolution of the western Central Qilian belt, Northwestern China, and constraints on convergent margin processes. *Gondwana Res.* 2017, 41, 301-324.